Polarization-controlled terahertz super-focusing

XiaoFei Zang,[1,2] ChenXi Mao,[1] XuGuang Guo,[1,2] GuanJun You,[1,2] He Yang,[1] Lin Chen,[1,2] YiMing Zhu,[1,2,a)] and SongLin Zhuang[1,2]

[1]*Terahertz Technology Innovation Research Institute, and Shanghai Key Lab of Modern Optical System, University of Shanghai for Science and Technology, No. 516 JunGong Road, Shanghai 200093, China*
[2]*Shanghai Cooperation Innovation Centre of Terahertz Spectroscopy and Imaging Technology, Shanghai 200093, China*

Metasurfaces have shown unprecedented capabilities in manipulating the phase, intensity, and polarization of electromagnetic waves. The coupling efficiency of surface plasmon polaritons is overcome by polarization sensitivity metasurfaces, but they face challenges in the application of high-intensity-based SPPs confined to the surface of a metal. Based on spiral arrays combined with a concentric groove, we experimentally demonstrate the application-oriented and polarization-controlled terahertz superfocusing by emitting high-efficiency radially convergent SPPs into free space to form a focal spot beyond the diffraction limit. The full wave at half maximum of the focal spot is 0.38λ, and it shows tunable intensity (the overall intensity of the focused spot can be tuned) by controlling the polarization state of the incident waves. This work paves a way towards imaging, data storage, and lithography. *Published by AIP Publishing.* https://doi.org/10.1063/1.5039539

Surface plasmon polaritons (SPPs) are evanescent surface waves that propagate along the dielectric-metal interfaces.[1,2] The manipulation of SPPs has open up avenues for the design of ultra-compact devices with a plethora of applications in integrated optical circuits.[3–8] Plasmonic lens, as important ultra-compact devices, have the capability of focusing SPPs into a tiny focal spot, holding promise for super-focusing, lithography, and data storage.[9–11] The traditional plasmonic lens is formed with a predefined annular slit embedded in a metal film. Upon the illumination of a vertical incident light, the slit boundaries serve as sub-sources (corresponding to propagating SPPs) that are interfered to a focal point.[12–14] Recently, great progress has been made in studying focusing properties under different kinds of polarized illuminations. For example, symmetry broken nanocorals and semicircular coupling grating are applied to focus linearly and circularly polarized light,[15,16] respectively, while the traditional annular slit is suitable for focusing radially polarized light.[17] Despite tremendous advances in the application of plasmonic lens, it is deficient in efficiency, which is most commonly caused by global geometry of the slit boundaries.[18,19]

Chiral metasurfaces (chiral plasmonic lens)[20] realized by embedding polarization-sensitive apertures in a metal film enable polarization-controlled directional coupling of SPPs, and thus they can create radially convergent SPPs with high conversion efficiency to overcome the above-mentioned limits. Thus far, chiral metasurfaces have been designed to shape and control the near-field focusing, directional SPPs focusing, spin-selective focusing, and so on.[21–25] However, most of the previous chiral plasmonic lens suffer from some intrinsic limits due to the focus confined on the surface of a metal. In this paper, we propose a polarization-dependent terahertz (THz) plasmonic lens consisting of chiral spiral arrays and a concentric groove, aiming to obtain application-oriented THz super-focusing (it is emitted into free space rather than confined on the metal surface). Since the chiral spiral array is polarization-dependent, it can be applied to control the intensity of the focal point, resulting in the intensity-tunable functionality. (The overall intensity of the focused SPPs can be tuned, rather than the size of the focal spot.) The detailed theoretical model of the intensity-tunable functionality is provided in the supplementary material, Sec. 1. The flexible and controllable THz super-focusing is of practical applications in many areas such as imaging, data storage, and lithography.

Figure 1 presents schematic of the designed structure for manipulating THz super-focusing. The whole lens is made up of two parts: a polarization-sensitive structure (PSS) and a concentric groove [Fig. 1(a)]. Two parallel Archimedes spiral slits separated with a distance of S are embedded in an aluminum plate to form the PSS and converge the excited SPPs into the center. The spiral array with geometrical charge can be mathematically described in cylindrical coordinates (R, θ)

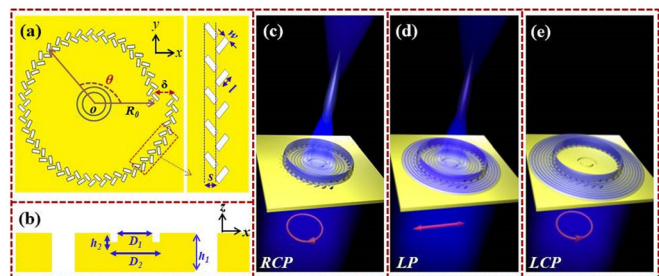$$R(\theta) = R_0 + \frac{\lambda_{spp}}{2\pi} \cdot \theta, \tag{1}$$

FIG. 1. Schematic diagrams of THz super-focusing: Structure of the THz plasmonic lens in the x-y plane (a) and the x-z plane (b). Super-focusing under the illumination of THz waves with right-hand polarization (RCP) (c), linear polarization (LP) (d), and left-hand polarization (LCP) (e).

a)Author to whom correspondence should be addressed: ymzhu@usst.edu.cn

where R_0 is initial radius and λ_{spp} represents the SPPs wavelength [$\lambda_{SPP} = \lambda\sqrt{\frac{\varepsilon_d + \varepsilon_m}{\varepsilon_m \varepsilon_d}} \approx 880\,\mu m$ ($\lambda = 880\,\mu m$), where λ is the incident wavelength, and ε_m and ε_d are the permittivity of metal and dielectric, respectively]. "+" determines a left-handed spiral array. A concentric groove is introduced to the center of the PSS to emit the convergent SPPs into free space, forming a focal point beyond the diffraction limit in free space. As a proof-of-concept, the geometric parameters selected are as follows: $R_0 = 5000\,\mu m$, $w = 250\,\mu m$, $l = 550\,\mu m$, $s = 220\,\mu m$, $h_1 = 550\,\mu m$, $h_2 = 100\,\mu m$, $D_1 = 1600\,\mu m$, $D_2 = 1800\,\mu m$, and $\delta = \lambda_{spp}$ [see Figs. 1(a) and 1(b)]. Both of these two Archimedes spiral arrays can excite SPPs, and the convergent SPPs toward the center of the structure are attributed to the interference between the excited SPPs.[19] Figures 1(c)–1(e) present schematic of polarization-dependent super-focusing: the intensity of the focal spot is gradually decreased when the polarization of the incident THz waves switch from right-hand polarization (RCP) to left-hand polarization (LCP) (see the theoretical model in the supplementary material, Sec. 1).

The mechanism of super-focusing is shown in Fig. 2. Figure 2(a) depicts the calculated result for the Archimedes spiral plasmonic lens (ASPL) under LCP illumination at $\lambda = 880\,\mu m$. The excited SPPs located on the surface of the ASPL are spread outward without penetrating the interior of lens. In contrast, for the RCP illumination, all of the SPPs propagate unidirectionally into the lens, showing a focal spot in the center [see Fig. 2(b)]. The focal spot (rather than donut field distribution) arises from the superposition of the spin and orbit angular momentum (OAM).[26] The right Archimedes spiral owns the geometrical charge of $l = -1$ (for RCP incidence) which can be considered as the quantum number of OAM. When the RCP (spin $\sigma = 1$) THz waves are impinged onto the ASPL, the total topological charge is $q = l + \sigma = 0$, leading to a focal spot in the center. Figure 2(c) shows the corresponding $|E_z|^2$ distributions in the x–z plane. It should be noted that most of the energy is just located on the surface of the aluminum plate, leading to intrinsic limits in practical applications. Therefore, a circular groove is introduced around the focal spot, and thus it can scatter the convergent SPPs into free space with the conversion efficiency of 0.77% in simulation (the definition of conversion efficiency is given in the supplementary material, Sec. 5) according to a certain angular

spectrum[27–29] [see Fig. 2(e)]. Here, the realization of THz super-focusing can be attributed to the scattering of SPPs into free space with in-phase field superposition, as shown in Fig. 2(e). In a word, the chiral spiral array captures the incident polarization-dependent THz waves into SPPs and converge them toward the center of the structure, while the groove is applied to scatter SPPs into a focal spot in free space. Figure 2(d) depicts the corresponding field distribution when a circular shaped groove is added into the plasmonic lens. Compared with Figs. 2(c) and 2(d), the focal spot confined to the surface of the metal [Fig. 2(c)] is scattered into free space [Fig. 2(d)], that is, 1.25 mm separated from the metal surface.

The inset in Fig. 3(a) shows the optical image of the sample. Traditional micromachining is applied to fabricate the slit array and groove. We experimentally explored unique characteristics of the plasmonic lens based on near-field scanning terahertz microscopy (NSTM) (see the supplementary material, Sec. 2). A collimated p-polarized THz wave radiated from a 100 fs ($\lambda = 780\,nm$) laser pulse pumped photoconductive antenna emitter is impinged on the sample. A commercial THz near-field probe with the resolution up to $20\,\mu m$ is functioned as a detector that is mounted on a translation stage to allow three-dimensional electric field scanning. The fiber-coupled probe is close to the sample to record the spatial electric field distribution of the focal spot, while the sample is fixed. The numerical simulations of the $|E_z|^2$ distributions are carried out by using the finite-different time-domain (FDTD) method [see Figs. 3(a) and 3(c)]. Here, we calculated the $|E_z|^2$ distributions of the focal spot at a distance of 1.25 mm away from the metal surface (because the groove is emitted from the focal spot into free space). Figure 3(a) demonstrates the focusing intensity [in the x-axis ($y = 0$) direction] of the focal spot under the illumination of THz waves ($\lambda = 880\,\mu m$) with different polarizations, i.e., RCP, REP (right-hand elliptically polarized), LP (linear polarized), LEP (left-hand elliptically polarized), and LCP. For RCP illumination, it shows the largest intensity of the focal spot with the full wave at half maximum (FWHM) of $337\,\mu m$ ($\approx 0.38\lambda$) that breaks the
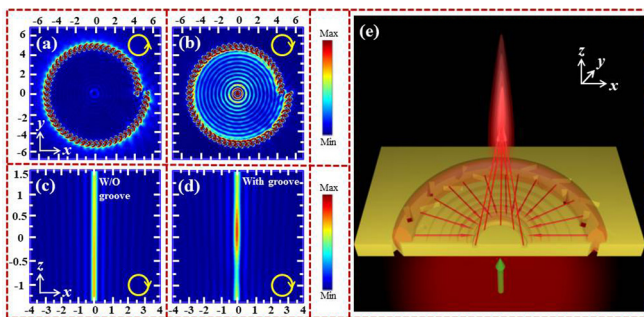

FIG. 2. (a) and (c) are the $|E_z|^2$ distributions for the plasmonic lens under the illumination of left-handed polarized (LCP) THz waves, while (b) is the case when right-handed polarized (RCP) THz waves impinge onto the sample. (d) The $|E_z|^2$ distributions for the plasmonic lens embedded with a groove for RCP illumination. (e) Schematic of the structure proposed to actualize super-focusing in free space. The length unit is millimeter.
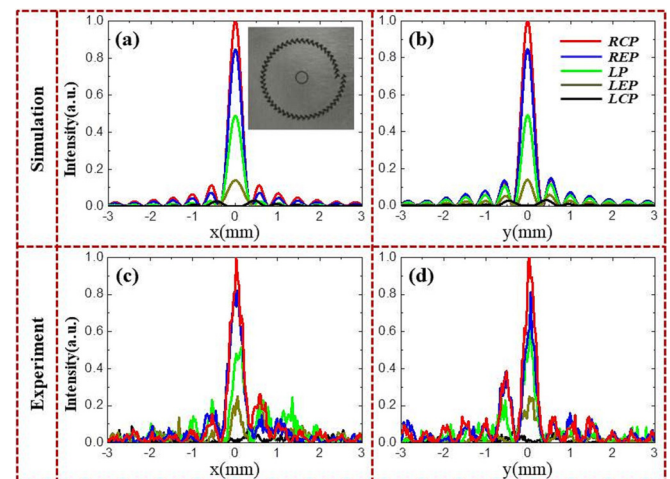

FIG. 3. Simulated (a) and measured (c) of the normalized $|E_z|^2$ distributions in the x-axis direction under different polarized THz waves: RCP (red), REP (blue), LP (green), LEP (brown), and LCP (black). (b) and (d) The corresponding simulated and measured $|E_z|^2$ distributions, respectively, in the y-axis direction. The inset is the sample.
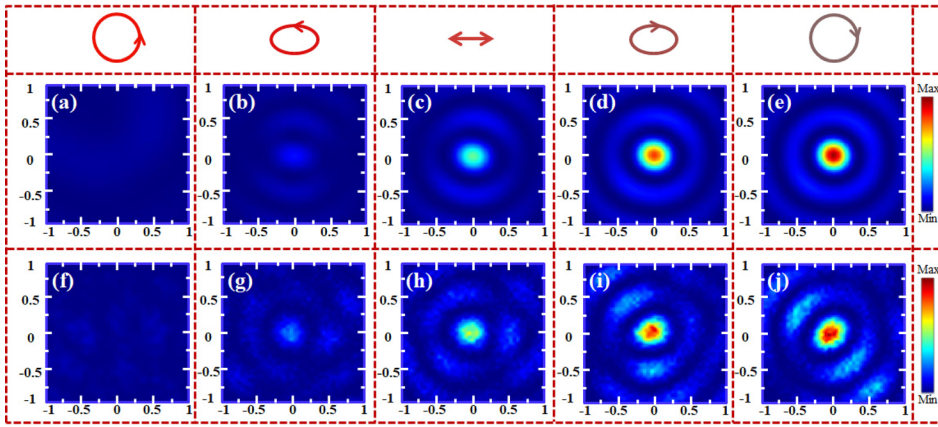
FIG. 4. The normalized $|E_z|^2$ distribution under the illumination of different polarized (in the first row) THz waves in the *x-y* plane: LCP [(a) and (f)], LEP [(b) and (g)], LP [(c) and (h)], REP [(d) and (i)], and RCP [(e) and (j)]. The images in the second row represent the simulated results, while the third row shows the measured results. The unit of length in millimeters.

diffraction limit. When the polarizations of the incident THz waves change from RCP to LCP, the intensity of the focal spot is gradually decreased to zero, demonstrating an intensity-tunable functionality. Figure 3(c) shows the corresponding measured results in the *y*-axis ($x = 0$). It not only reveals the intensity-tunable functionality but also shows the capability of super-focusing due to the 339 μm ($\approx 0.38\lambda$) of FWHM for the focal spot. Compared with Figs. 2(a) and 2(c), both the calculated and measured results show good agreement, except for a slight difference in FWHM and field distributions, which resulted from the fabrication errors (shape deformation of metal-slits and rough surfaces of the aluminium plate). The $|E_z|^2$ distributions in the *y*-axis are shown in Figs. 3(b) and 3(d), respectively. Under RCP illumination, the FWHM of the focal spot are 335 μm [Fig. 3(b)] and 317 μm [Fig. 3(d)] for the simulation and experiment, respectively. A slight discrepancy in FWHM between the *x*-axis and *y*-axis can be attributed to the asymmetric of the Archimedes spiral array in both directions. The focal properties of the spot with different groove parameters are also given in the supplementary material, Sec. 3.

The two-dimensional (*x*–*y* plane) electric field distributions of $|E_z|^2$ at $z = 1.25$ mm (a distance between the center of the focal spot and the metal surface) are illustrated in Fig. 4. In experiment, a THz quarter-wave plate was placed before the sample to generate the desired polarized THz waves, i.e., rotates the optical axis of THz quarter-wave plate to continuously obtain the circular-polarized, elliptical-polarized, and linear-polarized THz waves (see the supplementary material, Sec. 1). In Figs. 4(a)–4(e), the intensity of the electric field ($|E_z|^2$) is becoming stronger, which means that the overall intensity of the focal spot is tunable by modulating the polarization of the incident THz waves. The experimental demonstration of such unprecedented characteristic is shown in Figs. 4(f)–4(j). It can be found that the measured results are well consistent with the simulations, demonstrating the intensity-controllable THz super-focusing in the experiment. In addition, the electric field ($|E_z|^2$) distributions of the super-focusing in the *x*–*z* plane are also experimentally realized under different polarized incident THz waves (as shown in Fig. 5) to further demonstrate the intensity-tunable functionality. Figures 5(a)–5(e) illustrate the simulated results while Figs. 5(f)–5(j) show the corresponding measured field distributions (a slight mismatch between simulations and measurements can be attributed to the fabrication errors). The center

of the focal spot is located nearby $z = 1.25$ mm away from the metal surface, meaning that the groove emits radially convergent SPPs into the free space (with in-phase field superposition). The corresponding electric field ($|E_z|^2$) distributions in the *y*–*z* plane are shown in the supplementary material, Sec. 4.

Super-focusing, one of the most important methods for imaging, is commonly realized by annular/spiral slit embedded in a metal film under the illumination of radially polarized light. Compared with the linear-polarized light, the efficiency of directional SPPs excitation is much higher for the radially polarized light because of the constructive interference of the SPPs generated around the slit. However, the use of radially polarized light encounters challenge in generating it in the THz region due to the lack of THz SLM (spatial light modulator). The chiral plasmonic lens presented in this work features the functionality of converting the whole excited SPP into the focal spot under the illumination of right-hand circular-polarized THz waves. More importantly, a groove is introduced to emit the convergent SPP into free space to form a focal spot that arises from in-phase field superposition. Unlike the normal chiral plasmonic lens that just confines the focal spot onto the metal surface, the THz super-focusing (emitted in free space) in this work may own the practical applications in THz imaging. In addition, it is
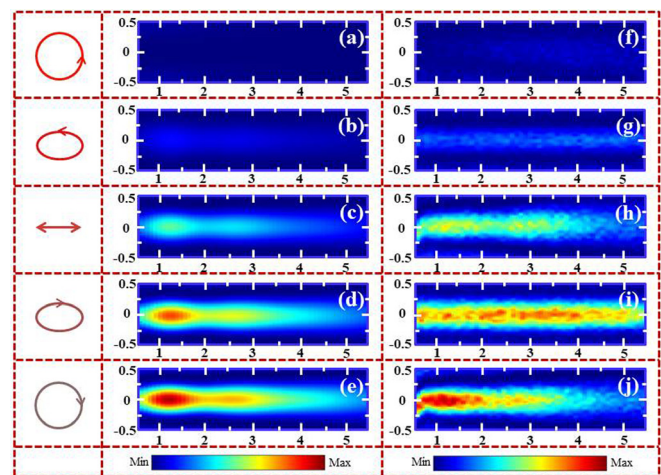

FIG. 5. The normalized $|E_z|^2$ distribution upon the illumination of different polarized (in the first line) THz waves in the *x-z* plane: LCP [(a) and (f)], LEP [(b) and (g)], LP [(c) and (h)], REP [(d) and (i)], and RCP [(e) and (j)]. The images in the second line represent the simulated results, while the third line shows the measured results. The unit of length in millimeters.

important to point out that the intensity of the focal spot is tunable by controlling polarization of incident THz waves. The methodology to generate the focal spot with intensity-tunable functionality provides a degree of freedom for modulating the focal spot (we also present a qualitative comparison of the performance between our device and the current state of the art in the supplementary material, Sec. 6). Although the polarization-controlled THz super-focusing in this work is demonstrated in the THz region, such an approach can be extended to the optical regime.[20,21] Therefore, it may have potential applications in optical data storage and lithography.[11]

In summary, we have proposed and experimentally demonstrated an approach to realize polarization-controlled THz super-focusing using an Archimedes spiral array combined with a groove. An intensity-tunable THz focal spot beyond the diffraction limit ($FWHM \approx 0.38\lambda$) was realized by controlling the polarization of the incident THz waves. Our approach solves several major issues associated with THz super-focusing: sub-wavelength of the THz focusing and intensity-tunable of the focal spot. Due to the robustness and simplicity of the design, it paves the way for future practical applications of imaging, data storage, and lithography.

See supplementary material for the theoretical model of the intensity-tunable functionality, near-field scanning terahertz microscopy (NSTM) system, focal properties with different groove parameters, electric field ($|E_z|^2$) distribution upon the illumination of different polarized THz waves in the y–z plane, and the performance of our device to the current state of the art.

[1]S. A. Maier, *Plasmonics: Fundamentals and Applications* (Springer, New York, 2007).

[2]H. Raether, *Surface Plasmons on Smooth and Rough Surfaces and on Gratings* (Springer, 1988).

[3]D. Y. Fedyanin, A. V. Krasavin, A. V. Arsenin, and A. V. Zayats, Nano Lett. **12**, 2459–2463 (2012).

[4]A. Kriesch, S. P. Burgos, D. Ploss, H. Pfeifer, H. A. Atwater, and U. Peschel, Nano Lett. **13**, 4539–4545 (2013).

[5]H. Shi, C. Du, and X. Luo, Appl. Phys. Lett. **91**, 093111 (2007).

[6]B. Jia, H. Shi, J. Li, Y. Fu, C. Du, and M. Gu, Appl. Phys. Lett. **94**, 151912 (2009).

[7]L. Chen, N. Xu, L. Singh, T. Cui, R. Singh, Y. Zhu, and W. Zhang, Adv. Opt. Mater. **5**, 1600960 (2017).

[8]L. Chen, Y. M. Wei, X. F. Zang, Y. M. Zhu, and S. L. Zhuang, Sci. Rep. **6**, 22027 (2016).

[9]W. L. Barns, A. Dereux, and T. W. Ebbesen, Nature **424**, 824–830 (2003).

[10]B. Gjonaj, A. David, Y. Blau, G. Spektor, M. Orenstein, S. Dolev, and G. Bartal, Nano Lett. **14**, 5598–5602 (2014).

[11]B. C. Stipe, T. C. Strand, C. C. Poon, H. Balamane, T. D. Boone, J. A. Katine, J. Liu, V. Rawat, H. Nemoto, A. Hirotsune, O. Hellwig, R. Ruiz, E. Dobisz, D. S. Kercher, N. Roberston, T. Albrecht, and B. Terris, Nat. Photonics **4**, 484–488 (2010).

[12]Z. W. Liu, J. M. Steele, W. Srituravanic, Y. Pikus, C. Sun, and X. Zhang, Nano Lett. **5**, 1726–1729 (2005).

[13]Y. Fu, W. Zhou, L. E. N. Lim, C. L. Du, and X. G. Luo, Appl. Phys. Lett. **91**, 061124 (2007).

[14]W. Chen, D. C. Abeysinghe, R. L. Nelson, and Q. W. Zhan, Nano Lett. **9**, 4320–4325 (2009).

[15]Z. Fang, Q. Peng, W. Wang, F. Hao, J. Wang, P. Nordlander, and X. Zhu, Nano Lett. **11**, 893–897 (2011).

[16]Y. Gorodetski, A. Niv, V. Kleiner, and E. Hasman, Phys. Rev. Lett. **101**, 043903 (2008).

[17]G. M. Lerman, A. Yanai, and U. Levy, Nano Lett. **9**, 2139–2143 (2009).

[18]M. Zhao, J. Du, H. Shi, S. Yin, L. Xia, B. Jia, M. Gu, and C. Du, Opt. Express **18**, 14664–14670 (2010).

[19]G. Spektor, A. David, B. Gjonaj, L. Gal, G. Bartal, and M. Orenstein, Opt. Express **24**, 2436–2442 (2016).

[20]J. Lin, J. P. Balthasar Mueller, Q. Wang, G. Yuan, N. Antoniou, X. C. Yuan, and F. Capasso, Science **340**, 331–334 (2013).

[21]G. Spektor, A. David, B. Gjonaj, G. Bartal, and M. Orenstein, Nano Lett. **15**, 5739–5743 (2015).

[22]S. Lee, K. Kim, S. Kim, H. Park, K. Kim, and B. Lee, Optica **2**, 6–13 (2015).

[23]J. Liu, Y. Gao, L. Ran, K. Guo, Z. Lu, and S. Liu, Appl. Phys. Lett. **106**, 013116 (2015).

[24]J. Li, P. Tang, W. Liu, T. Huang, J. Wang, Y. Wang, F. Lin, Z. Fang, and X. Zhu, Appl. Phys. Lett. **106**, 161106 (2015).

[25]G. Lee, S. Lee, H. Yun, H. Park, J. Kim, K. Lee, and B. Lee, Sci. Rep. **6**, 33317 (2016).

[26]C. Chen, C. Ku, Y. Tai, P. Wei, H. Lin, and C. Huang, Nano Lett. **15**, 2746–2750 (2015).

[27]L. Yu, D. Lin, Y. Chen, Y. Chang, K. Huang, J. Liaw, J. Yeh, and C. Lee, Phys. Rev. B **71**, 41405 (2005).

[28]F. López-Twjeira, F. García-Vidal, and L. Martín-Moreno, Phys. Rev. B **72**, 161405 (2005).

[29]A. Nikitin, F. López-Twjeira, and L. Martín-Moreno, Phys. Rev. B **75**, 35129 (2007).